Nanoscale

Metal-Organic Framework Derived 3D Graphene Decorated NaTi2(PO4)3 for Fast Na-ion Storage

Journal:	*Nanoscale*
Manuscript ID	NR-ART-01-2019-000610.R1
Article Type:	Paper
Date Submitted by the Author:	10-Mar-2019
Complete List of Authors:	Wang, Lei; Harbin Institute of Technology Huang, Zhennan; University of Illinois at Chicago, Mechanical & Industrial Engineering Wang, Bo; Harbin Institute of Technology, Luo, Hao; Harbin Institute of Technology Cheng, Meng; University of Illinois at Chicago, Department of Mechanical and Industrial Engineering Yuan, Yi-fei; University of Illinois at Chicago He, Kun; University of Illinois at Chicago, Mechanical and Industrial Engineering Foroozan, Tara; University of Illinois at Chicago Deivanayagam, Ramasubramonian; University of Illinois at Chicago, Mechanical and Industrial Engineering Liu, Guijing; Ludong University Wang, Dianlong; Harbin Institute of Technology, MIIT Key Laboratory of Critical Materials Technology for New Energy Conversion and Storage, School of Chemistry and Chemical Engineering Shahbazian-Yassar, Reza; University of Illinois at Chicago, Mechanical and Industrial Engineering

Cite this: DOI: 10.1039/c0xx00000x

www.rsc.org/xxxxxx

PAPER

Metal-Organic Framework Derived 3D Graphene Decorated $NaTi_2(PO_4)_3$ for Fast Na-ion Storage

Lei Wang [a,b], Zhennan Huang [b], Bo Wang [a,*], Hao Luo [a], Meng Cheng [b], Yifei Yuan [b], Kun He [b], Tara Foroozan [b], Ramasubramonian Deivanayagam [b], Guijing Liu [c], Dianlong Wang [a,*], Reza Shahbazian-Yassar [b,*]

Received (in XXX, XXX) Xth XXXXXXXXX 20XX, Accepted Xth XXXXXXXXX 20XX
DOI: 10.1039/b000000x

NASCION-type materials featuring super ionic conductivity are of considerable interest for energy storage in sodium ion batteries. However, the issue of inherent poor electronic conductivity of these materials represents a fundamental limitation in their utilization as battery electrodes. Here, for the first time, we develop a facile strategy for the synthesis of NASICON-type $NaTi_2(PO_4)_3$/reduced graphene oxide (NTP-rGO) Na-ion anode material from three-dimensional (3D) metal-organic frameworks (MOFs). The selected MOF serves as an *in-situ* etching template for the titanium resource, and importantly, endows them with a structure-directing property for the self-assembly of graphene oxide (GO) through a one-step solvothermal process. Through the subsequent carbonization, rGO decorated NTP architecture is obtained, which offers fast electron transfer and improved Na^+ ion accessibility to active sites. Benefiting from its unique structural merits, the NTP-rGO exhibits improved sodium storage properties in terms of high capacity, excellent rate performance and good cycling life. We believe the findings of this work provide new opportunity to design high performance NASICON-type materials for energy storage.

Introduction

Advanced energy storage technologies are critical for widespread utilization of renewable energy sources[1-3]. Although lithium-ion cells have gained great improvement in energy density and life time, they still face scale up challenges as a result of the limited Li resources and high processing cost. Battery chemistries based on intercalation of Na^+, K^+, Mg^{2+}, and Zn^{2+} have been widely regarded as alternative candidates because of their abundance and environmental friendliness[4-8]. Among the aforementioned battery candidates, sodium ion batteries (SIBs) are particularly promising energy storage devices that could complement or even replace lithium-ion batteries for large-scale applications[9-11]. Nevertheless, effects of the larger radius of Na^+ (0.102 nm) than that of Li^+ (0.069 nm) will likely limit their development, and dictate against their use in stationary energy storage, where its poor Na^+ movement and severe volume expansion of the host materials lead to poor rate capability and cycle stability[12-13]. Therefore, it is still a vital requirement to develop appropriate electrodes with suitable microstructures and high reversibility for SIBs.

Several theoretical and experimental studies have verified that NASICON-type materials with open 3D framework can act as outstanding electrode materials with high ionic conductivity and electrochemical stability[14-17]. Their general formula is $A_mB_2(XO_4)_3$, where A represents an alkali ion (Li^+, Na^+, etc.), B is a transitional metal ion (V^{5+}, Ti^{4+}, or Fe^{3+}, etc.), and X is any one of the following ions: Si^{4+}, P^{5+}, S^{6+}, Mo^{6+}. $A_mB_2(XO_4)_3$ features two BO_6 octahedra and three PO_4 tetrahedra connected by corner-sharing. The NASICON-type structure provides abundant ions with intercalation active sites of A (1) and A (2) based on the alkali content ($n \leqslant 1$ or $n>1$) and more importantly, allows the easy migration of the ions between A (1) and A (2). Some examples include $Na_3Fe_2(PO_4)_3$[18], $Na_3V_2(PO_4)_3$[19] and $NaZr_2(PO_4)_3$[20]. However, previous attempts are plagued by deficient performance of $A_mB_2(XO_4)_3$ materials due to the intrinsic poor electron transport. A general strategy is to introduce carbon materials in the form of carbon shells, reduced graphene oxide (rGO), carbon nanotubes (CNTs) etc. into NASICON-type structure materials to maximize electrical conductivity[21-23]. Among those, two dimensional (2D) rGO with large surface area, high conductivity, mechanical and chemical stability is an ideal choice[24-25]. Thus, considerable effort has been dedicated to the design and fabrication of $A_mB_2(XO_4)_3$/rGO composites[26]. Despite great progress, there are still many issues that must be overcome for further successful advancement in this area. One main issue is the unsatisfactory contact between $A_mB_2(XO_4)_3$ and rGO. Moreover, rGO could undergo agglomeration due to strong intersheet p–p interaction during synthesis, which does not allow high ion accessibility[27]. Therefore, developing a new and effective approach for controlled incorporation of rGO

into NASICON type materials to overcome their drawbacks is highly desired.

Metal-organic frameworks (MOFs), a new class of porous crystalline materials constructed by coordination of metal ions/clusters with polytopic organic ligands, have recently emerged as ideal precursors for the development of electrode materials for energy conversion and storage because of their large surface area, tunable porosity and controllable structures[28-30]. To our best knowledge, however, the preparation of NASICON type structure materials composited with rGO prepared from MOFs appears unreported. NASICON type $NaTi_2(PO_4)_3$ (NTP) is usually considered as an excellent anode for SIB because of its low working voltage vs. Na^+/Na. Herein, for the first time, we demonstrate the preparation of the NTP-rGO composites by using a titanium-based metal-organic frameworks (MIL-125) as the precursor from the solvothermal process. The selected MOF serves as an *in-situ* etching template for the titanium resource, and importantly, endows them with a structure-directing property for the self-assembly of graphene oxide (GO). The rGO decorated NTP microspheres are obtained from the subsequent carbonization. This robust architecture not only owns electron transport channels to enable high electrical conductivity, but also favors facile sodium-ion pathways that render fast, reversible de-intercalation/intercalation processes. Furthermore, the assembled microspheres with increasing interlayer distance of NTP-rGO nanocomposites could significantly accommodate the expansion during insertion of Na ions. As a result, NTP-rGO delivers a combination of large capacity (129.2 mAh g^{-1}), high rate performance (77% retention under the 500-fold increase in current densities) and long-term cycling stability (92.0 mAh g^{-1} retention after 1000 cycles). The proposed strategy is expected to provide other $A_mB_2(XO_4)_3$/rGO materials with a significantly improved performance for energy storage.

Experimental

Material and Synthesis

The synthesis of titanium-organic framework (MIL-125) was based on the previous report with some revisions. Typically, 3.0 g terephthalic acid and 1.55 ml Titanium(IV) isopropoxide were dissolved in the mixed solution containing 6 ml dried methyl alcohol and 54 ml dimethylformamide. After stirring at room temperature, the mixture was transferred into a 100 ml stainless steel cylinder with a Teflon liner and heated at 150 °C for 24 h. After cooling down, the white product was collected by centrifugation and thoroughly washed with methyl alcohol.

NTP-rGO (also named as NTP-rGO-20) was synthesized by the hydrothermal reaction and subsequent annealing treatment. Firstly, a mixture was obtained by adding 20 mg GO and 0.25 ml H_3PO_4 in 4.25 ml deionized water. Then, 250 mg $NaH_2PO_4{\cdot}H_2O$ was dissolved in the above mixture, followed by addition of 615 mg MIL-125. The suspension was thereafter poured into a 50 ml Teflon-liner steel autoclave and heated at 150 °C for 2 hours. The resultant product was achieved by centrifugation, thoroughly washed with ethanol and dried at 50 °C overnight. Annealing under flowing argon atmosphere was performed in a tubular furnace at 700 °C for 4 h, with a ramp rate of 5 °C min^{-1}. After naturally cooling to room temperature, NTP-rGO powder was obtained. The control samples prepared with different GO additive amount of 10 mg and 30 mg were named as NTP-rGO-10 and NTP-rGO-30, while other synthesis conditions were kept the same. Moreover, NTP precursors were synthesized by the hydrothermal reaction of mixture without GO addition. The samples fabricated with different hydrothermal reaction time of 10 min, 30 min and 4 h were designated as NTP-10m, NTP-30m and NTP-4h. Thermogravimetric analysis (TGA) shows that the carbon contents of NTP, NTP-rGO-10, NTP-rGO and NTP-rGO-30 are about 1.8 wt%, 4.0 wt%, 4.9 wt% and 6.5 wt%, respectively (**Fig. S1**†).

Characterization

The morphologies and microstructures of these samples were first studied with the JEOL JSM-6320F field emission scanning electron microscope (FESEM), JEOL JEM-ARM200CF transmission electron microscopy (TEM). The crystallographic phases were characterized by X-Rigaku D/max-γB X-ray diffraction with a 2θ ranging from 10 to 90°. X-ray photoelectron spectroscopy (XPS) studies were conducted with PHI 5700 ESCA System to study the surface chemical structure composition. The *in-situ* TEM characterization was performed in JEOL-3010 TEM (3000 kV). The Au rod was mounted on the Nanofactory electrical biasing holder, which was used to dip the NTP materials. A tungsten (W) rod was used to scratch Na metal to obtain fresh Na in the glove box and then taken out to expose to air for 5s. It would form the Na_2O layer on the surface as the native solid electrolyte. After inserting into the TEM column, the Na/Na_2O side was contacted with the NTP through piezo control. The bias of -3V was applied on the nanoparticles versus the Na metal to initiate the sodiation process. Additional details on the *in-situ* TEM studies of battery materials can be found at the previous work[31-34].

Electrochemical measurements

The electrochemical properties were evaluated at room temperature by sodium half cells assembled in the glovebox. The slurry of the working electrode was prepared by blending a powder mixture consisting of NTP, carbon black and polyvinylidene difluoride (PVDF) with a mass ratio of 8:1:1 in some N-methyl-2-pyrrolidone (NMP). The homogeneous slurry was spread on a piece of copper foil, followed by being transferred into a vacuum oven at 120 °C for 12 h. The working electrodes were fabricated by cutting the copper foil into disks with diameter of 15 mm. Coin-type cells (CR2032) were assembled with sodium foil as the counter electrode, glass fiber as the separator and 1 M $NaClO_4$ dissolved in a mixture of ethylene carbonate (EC) and propylene carbonate (PC) in a volume ratio of 1:1 as electrolyte. The specific capacity of electrode materials was calculated from galvanostatic charge-discharge (GCD) tests and the details are provided in **ESI**†. The average loading mass of active material was about 1.53 mg. The rate performance and cyclic performance were tested using a Neware BTS4000 battery testing system. The data of the cyclic voltammetry (CV) and electrochemical impedance spectroscopy

(EIS) were collected by CHI 660E electrochemical workstation. CV tests were carried out at a scanning rate of 0.1 mV s^{-1} within a voltage window of 1.5-3.0 V (vs Na/Na^+). The EIS measurement was performed by fresh cells from 10 mHz to 100 kHz. ZSim Demo software was used to fit the data.

Results and discussion

The NTP precursor was synthesized from MIL-125 via a facile solvothermal process. Schematic illustration (**Fig. 1a**) combined with time-dependent tests were provided to gain insight into the evolution of the structure. Here, a key innovation is that MIL-125 was used as the self-sacrificing template to prepare the NTP precursor. The elementary composition and phase purity of the MIL-125 were confirmed by X-ray photoelectron spectroscopy (XPS) and X-ray diffraction analysis (XRD) (**Fig. S2† and S3†**). Scanning electron microscopy (SEM) images (**Fig. 1b and 1c**) reveal that MIL-125 owns uniform morphology with sizes in the range of 1-2 μm. Furthermore, MIL-125 crystallites feature large specific surface area of 1083.2 m^2 g^{-1} and a large number of micropores along with hierarchical pore structure (**Fig. S4a† and S4b†**). This pore size distribution could provide the balance of reaction ion diffusion kinetics and concentration gradient. In this system, the abundant ions serve dual roles (etching-like agents and Na^+/PO^{4-} sources), which are responsible for the construction of edge site-enriched network structure based on the template etching and coprecipitation mechanisms[35]. **Fig. 1d-g** show the SEM images of the NTP precursor with different reaction time. The precursor nanosheets in a well-retained two-dimensional (2D) morphology with uniform thickness of ~15-20 nm can be orderly stacked into microsphere structures under the 2 h reaction time (**Fig. 1f and S5†**). The transmission electron microscopy (TEM) image (**Fig. S6a†**) further reveals that the restacked nanosheets are assembled into microspheres. For comparison, SEM images of NTP-10m and NTP-30m (**Fig. 1d and 1e**) show that the less NTP sheets are formed, while a large amount of structural breakdown is visible under the longer reaction time (**Fig. 1g**). According to the above analysis, the formation mechanism of NTP microspheres precursor could be described as follows. Under solvothermal conditions, the H^+ protons derived from the addition of H_3PO_4 could break MIL-125 bonds resulting in liberated Ti^{2+} ions. The protons could carve the crystal consistently along the fixed edge directions. Simultaneously, the continuous inward diffusion of Na^+ and PO^{4-} ions from the concentration gradient react with liberated Ti^{2+} ions to generate NTP nanoplates on the surface of the framework. As a result, the NTP precursor nanosheets with a similar angle are assembled into microspheres.

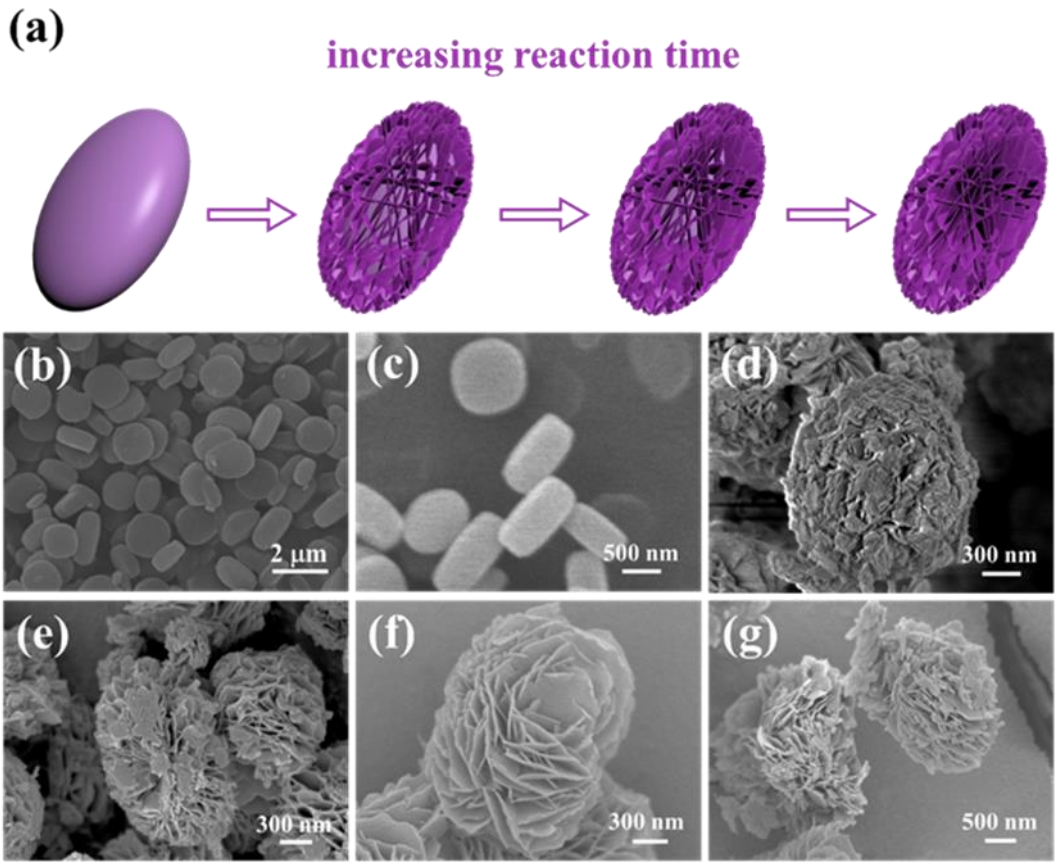

Fig. 1 a) Schematic illustration of the fabrication process of the NTP precursor; b) and c) SEM images of the MIL-125; d-g) SEM images of the NTP precursor with different reaction time d) 10 min, e) 30 min, f) 2 h and g) 4 h.

The synthesis of the NTP-rGO precursor from MIL-125 is presented in **Fig. 2a**. GO-anchored NTP could be prepared through an electrostatic attraction process by coassembly of negatively charged GO and positively charged liberated Ti^{2+} ions on the edge of MIL-125 formed from template etching process. The TEM images of NTP-rGO precursor at low magnification (**Fig. 2b and S6b†**) show the morphology of microspheres, resembling sea urchins, with a particle size ranging from 1-2 μm, which are assembled by the interweaved nanosheets. The magnified TEM images (**Fig. 2c and 2d**) reveal that rGO are homogenously

assembled into NTP architecture without obvious aggregation. No unassembled irregular rGO nanosheets can be observed perhaps due to the strong electrostatic attraction, indicating the superiority of such hydrothermal and H^+ induced assembly method based on MIL-125 materials. After subsequent carbonization treatment, it is noted that NTP-rGO shows the similar sea urchins-like shapes as same as the obtained NTP samples (**Fig. 2e, S6c† and S6d†**). The corresponding elemental mappings clearly confirm that C, Na, O, P, Ti atoms are highly uniformly distributed throughout the sample (**Fig. 2h**), suggesting the successful synthesis of NTP-rGO. The high-resolution TEM (HRTEM) image in **Fig. 2f** and **Fig. S7†** displays obvious differences of the morphology for rGO and NTP, in which the interplanar spacings of 0.609, 0.304, 0.424, 0.348 and 0.245 nm correspond to the (012), (024), (110), (202), (300) facets of NTP, respectively. High-resolution high-angle annular dark-field (HAADF) scanning transmission electron microscopic (STEM) was performed to verify the detailed crystal structure of NTP material, including the atomic-resolution information about the crystal lattice and the order of the phases (**Fig. 2g**). The lattice fringe is nearly 4.3 Å corresponding to the interplanar distance of the NTP (110) plane to confirm the crystalline structure.

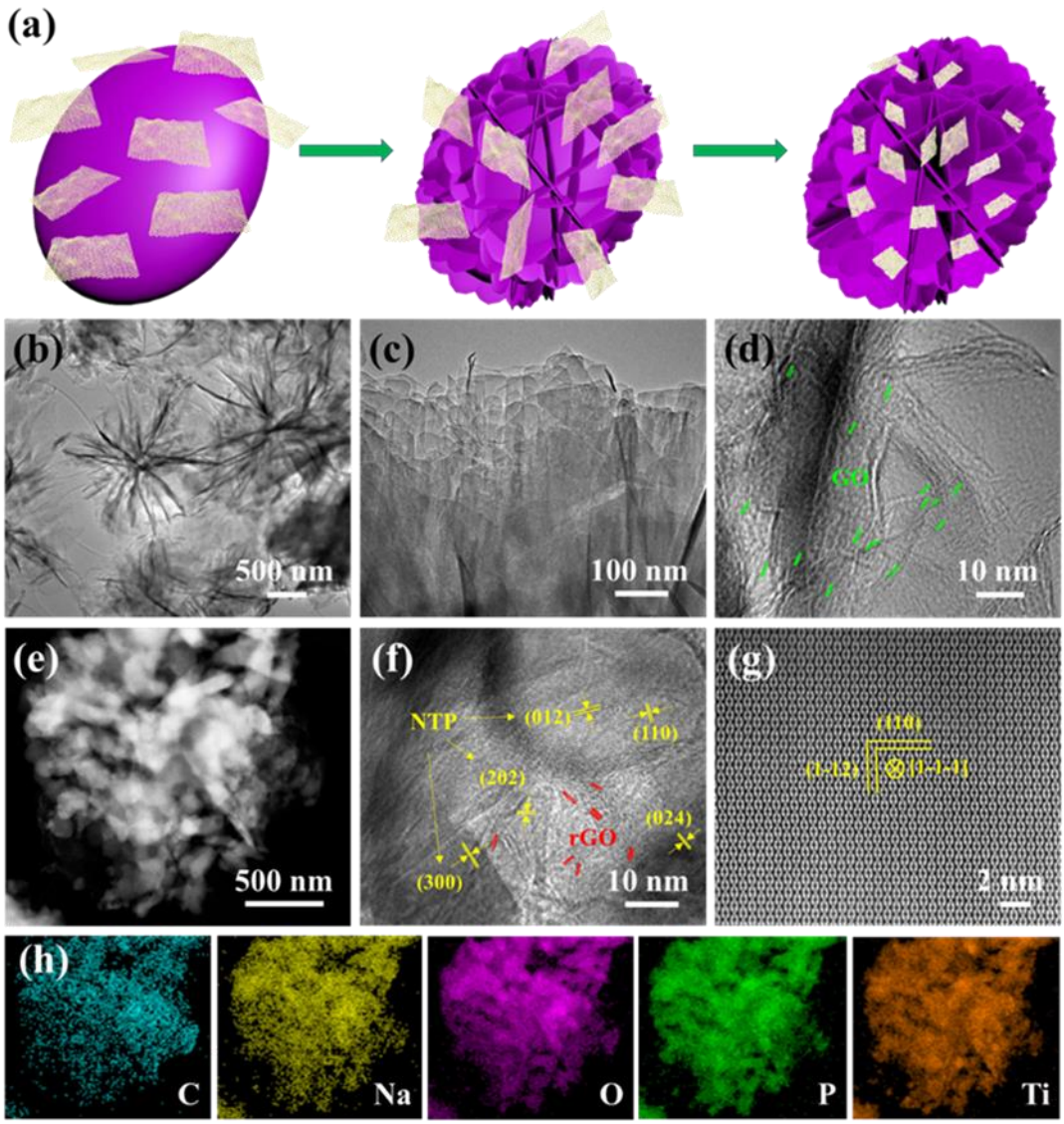

Fig. 2 a) Schematic illustration of the self-assemble process of the NTP-rGO; b-d) TEM and HRTEM images of NTP-rGO precursor; e) STEM-HAADF image of NTP-rGO; f) HRTEM image of NTP-rGO; g) Atomic-resolution STEM-HAAD image of NTP-rGO; h) The corresponding elemental (C, Na, O, P, Ti) mappings of the same region in Fig. 2e.

Fig. 3a shows the powder X-ray diffraction (XRD) analysis of the resultant product, where all the characteristic diffraction peaks can be indexed as NTP (JCPDS Card No. 33-1296) with an $R\bar{3}c$ space group (167). No diffraction peaks attributed to rGO can be observed, presumably because of the low contents and/or inherent defective structure. Based on Rietveld refinement, the calculated lattice parameters of *a* and *c* are 8.4940 Å and 21.8447 Å, respectively, which are close to the previous reported values, suggesting a good crystal structure and high purity (**Fig. S8†**)[36]. However, Raman spectra reveals pronounced two characteristic peaks loaded at around 1339 and 1587 cm^{-1}, attributing to the D (disordered carbon) and G (graphitized carbon) bands (**Fig. 3b**). In general, the D peak associates with sp^3-hybridized carbon and the G peak suggests the vibration in all sp^2-band carbon atoms in a

two-dimensional hexagonal lattice[37]. The D-band and G-band have also been detected in the NTP sample, which perhaps resulted from the residual organic ligands of MIL-125 during sintering process [38]. Furthermore, the lower peak intensity ratio of (I_D/I_G) indicates the higher degree of graphitization[39]. The calculated I_D/I_G of NTP-rGO (1.05) is lower than that of NTP (1.13), demonstrating that the thermally reduced state of rGO has a greater degree of graphitization resulting in an enhanced electrical conductivity[40].

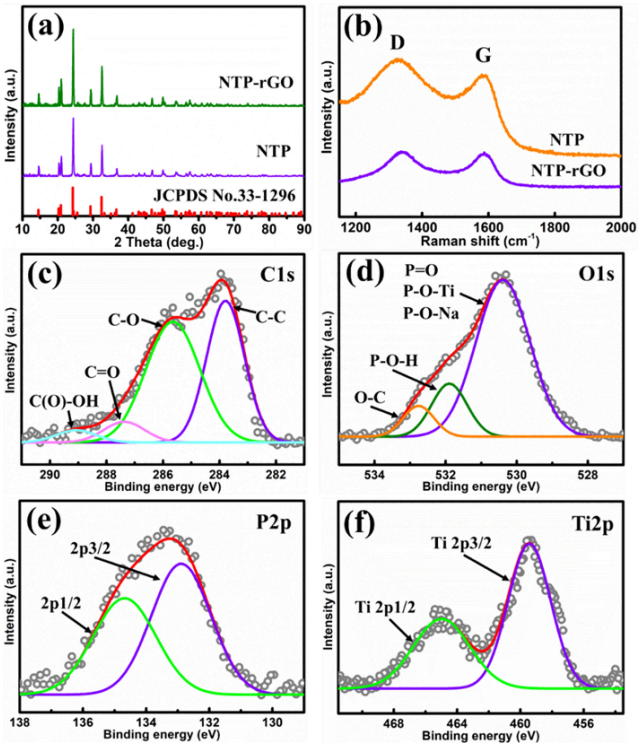

Fig. 3 a) XRD patterns of the samples; b) Raman spectra of the samples; c-f) High-resolution spectra for c) C 1s, d) O 1s, e) P 2p, and f) Ti 2p of the NTP-rGO.

To investigate the main components in NTP-rGO, this sample was further characterized by the XPS. The XPS signal in wide scan survey spectra clarifies the binding environments of Na, Ti, O, P and C elements in NTP-rGO sample (**Fig. S9**†), which is in good agreement with the elemental mapping result. An obvious C 1s peak is observed for NTP-rGO at about 284 eV (**Fig. 3c**), which can be deconvoluted into four components at 283.8, 285.7, 287.4 and 289.1 eV, being coincident with that of oxygen-containing functional groups of C-O, C=O and O-C=O bonds respectively. The O 1s peak in **Fig. 3d** can be resolved into three components centered at 532.8, 531.9, and 530.4 eV. The peak centered at 530.4 eV could be assigned to Ti-O-P, Na-O-P and P=O, the peak at 531.9 eV corresponds to O in P-O-H, and the peak at 532.8 ascribes to the C-O bonds[41]. The P 2p XPS spectrum can be deconvoluted into two peaks at 134.7 and 132.9 eV with an area ratio of about 1 to 2 (**Fig. 3e**), corresponding to binding energies for P $2p_{1/2}$ and P $2p_{3/2}$. The Ti 2p spectrum is well fitted by two peaks at 465.0 and 459.4 eV, corresponding to the Ti $2p_{1/2}$ and Ti $2p_{3/2}$ spin-orbital splitting photoelectrons in the Ti^{4+} chemical states (**Fig. 3f**). For comparison, XPS test of NTP was conducted and the obtained result is shown in **Fig. S10**†. The Ti 2p peak position variation can manifest the proper interactions between rGO and NTP[39]. It can be observed that the binding energy of NTP-rGO presents a negative shift of 0.8 eV compared with that of NTP, exhibiting the chemical interaction between the NTP and rGO[42]. The rGO sheets serve as excellent electron acceptors, therefore, the close contact between NTP and rGO can provide effective electron transfer channels for NTP-rGO[43].

The electrochemical performance of NTP composite electrodes were studied by coin-type half-cell assembly using sodium metal as counter electrode. The NTP-rGO composites constructed with highly conductive rGO leads to significant improvement in specific capacity and coulombic efficiency (CE). **Fig. 4a** presents the first cycle of discharge/charge profiles of the two samples at a current density of 0.1 C between 1.5-3 V *vs.* Na/Na^+. Although the well-defined, flat and symmetric charge/discharge voltage plateaus are observed in the two electrodes, there is obvious distinction in discharge/charge polarization. Note that the first discharge plateau of NTP-rGO sample is about 2.11 V, and the corresponding charge plateau is around 2.15 V, resulting in a much smaller polarization of 39 mV than that of NTP (145 mV). Such decreased discharge/charge polarization is attributed to the improved electron conductivity resulted from the unique structure. Thus, the NTP-rGO anode achieves the high first discharge and charge capacities of 133.3 and 129.1 mAh g^{-1}, respectively, corresponding to a CE of 96.8%. It is worth stressing that the CE is obviously higher than that of the previous reported NTP composites (**Table S1**) [21, 44-48].

To further explore the influence of the rGO on the electrochemical performance, the cyclic voltammetry (CV) was conducted at 0.1 mV s^{-1} with a voltage range from 1.5 V to 3.0V (**Fig. 4b**). A pair of well-defined characteristic redox peaks of the NTP-rGO and NTP samples can be observed, which exhibits the representative Ti^{3+}/Ti^{4+} redox reaction in every first cycle of the two samples, corresponding to the Na^+ de-intercalation/re-intercalation process: $NaTi_2(PO_4)_3 + 2Na^+ + 2e^- \leftrightarrow Na_3Ti_2(PO_4)_3$[49-51]. However, obvious distinction in the position and intensity of the peaks can be clearly seen among the samples. The NTP-rGO displays the lower potential interval between the reduction and oxidation peaks (190 mV) compared with the NTP (350 mV), suggesting better reversibility and optimized electrode kinetics in accordance with the discharge/charge curves. Moreover, the higher current responds and larger integrated area for NTP-rGO demonstrate the increased capacity, further indicating that the rGO assembling into NTP is responsible for improved battery performance. Because the Na^+ insertion/extraction process is a typical diffusion-controlled behavior, the peak current (I_p) of the CV curve can be calculated based on the following formula[52]:

$$I_p = 2.69 \times 10^5 n^{3/2} A C D^{1/2} V^{1/2} \quad (1)$$

Where n is the number of exchange electrons, A is the active surface of the anode, C is the concentration of Na^+ in the anode, V is the scanning rate, and the Na^+ diffusion coefficient (D) is proportional to $I_p^{-1/2}$. According to the order of current, it can be deduced qualitatively that NTP-rGO anode achieves the highest D value. The result implies that NTP-rGO composite has the best ability of sodium-ion transmission.

As a proof of the boosted electrochemical behavior for the NTP-rGO electrode, the electrochemical impedance

spectroscopy (EIS) was performed and the Nyquist plots are displayed in **Fig. 4c**[53]. Both of the Nyquist plots demonstrate a depressed semicircle in the high frequency range and a steep line in the low frequency region[54]. The charge-transfer resistance (R_{ct}) indicating the electronic conductivity of the active material and diffusion capability of the sodium ions at the electrode-electrolyte interface, which is calculated based on the diameter of the semicircle[55]. Apparently, the Rct value of the NTP-rGO (177.3 Ω) is far smaller than that of NTP (1157.6 Ω), suggesting that the NTP-rGO structure is advantageous in providing a faster charge transport. On the other hand, the Warburg resistance related to the straight slope correspond to the Na^+ diffusion in the active material (D_{Na+}) and can be calculated as the following equation[56]:

$$D_{Na^+} = R^2T^2/2A^2n^4F^4C^2\sigma^2 \quad (2)$$

Except for the constants including the surface area of the electrode (A), the number of electrons per molecule during oxidization (n), the Faraday constant (F), the concentration (C), the gas constant (R) and the absolute temperature (T), the Warburg factor (σ) is related to Z_{re} ($Z_{re} \propto \sigma\omega^{-1/2}$)[57]. **Fig. 4d** shows the relation plot between Z_{re} and $\omega^{-1/2}$, which is used to calculate σ and D_{Na+}. According to the order of the σ values for NTP (287.7) < NTP-rGO (23.5), the D_{Na+} of the NTP-rGO is larger than that of NTP. Furthermore, the battery performance of NTP-rGO composites are highly affected by the added amount of GO in the solvothermal process. Based on the electrochemical tests, NTP-rGO electrode with 20 mg GO addition is found to exhibit the best battery performance among these electrodes (**Fig. S11**†).

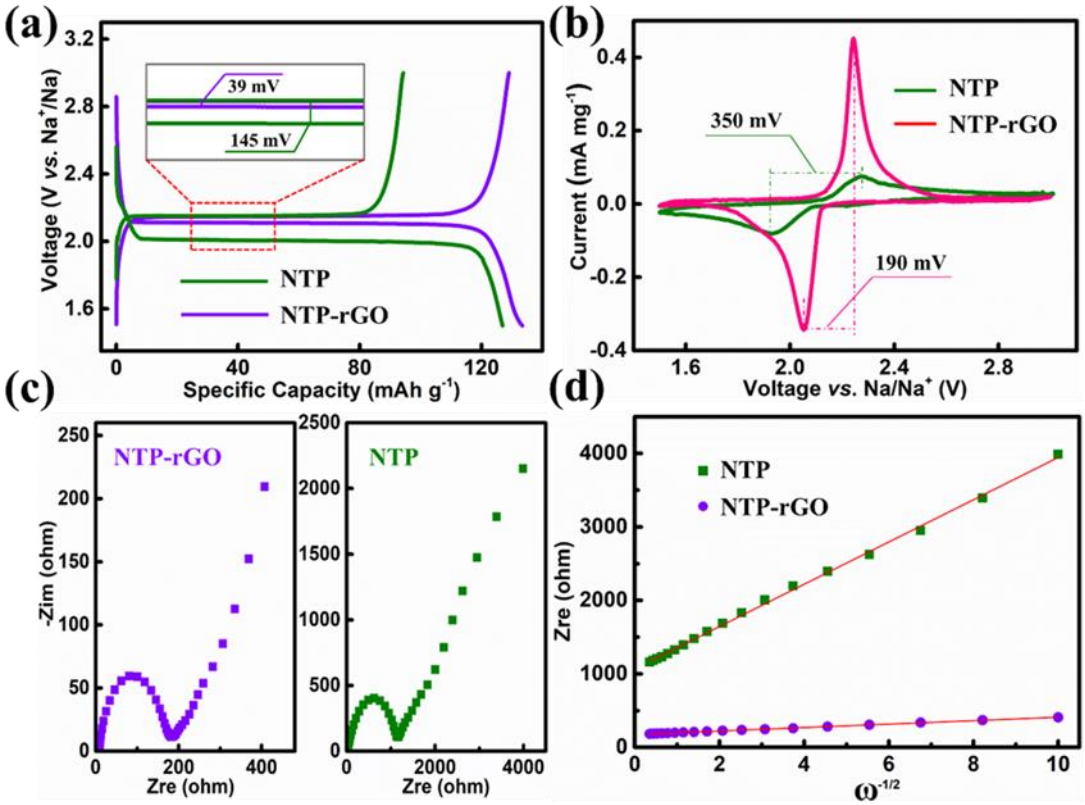

Fig. 4 a) First cycle of the galvanostatic charge-discharge profiles of the samples at 0.1 C; b) First cycle of CV curves of the samples under the scan rate of 0.1 mV s^{-1}; c) Nyquist plots; d) Corresponding Z_{re} plots against the reciprocal square root of the angular frequency.

The NTP-rGO anodes shows impressive electrochemical properties in term of sodium storage. **Fig. 5a** displays the rate performance of NTP-rGO at various current rates from 0.1 C to 50 C. The reversible discharge capacity is 129.2 mAh g^{-1} at a current density of 0.1 C and retains 99.4 mAh g^{-1} at 50 C. A comparison of specific capacity and rate performance of the NTP-rGO with previously reported NTP composite electrode is presented in **Fig. S12**†. Such values for NTP-rGO exceeds that of the most previous reported NTP composites materials. Remarkably, after 56 cycles under the different current densities, the discharge capacity can still recover to 128.3 mAh g^{-1} when the current rate returns to 0.1 C. Compared with NTP-rGO electrode, the NTP electrode exhibits a poor rate-performance and the discharge capacity is just 95.8 mAh g^{-1} at 0.1 C. The sharp decline in discharge capacity of NTP results from the unsatisfied electrical conductivity, which is in accordance with the EIS results. The galvanostatic discharge-charge curves of the NTP-rGO at various current densities are shown in **Fig. 5b**. It can be clearly observed that flat and symmetric charge/discharge voltage plateaus are distinguishable even if at high current rate of 50 C, suggesting that the NTP-rGO can rapidly complete the charge/discharge process within several minutes. Furthermore, an additional plateau around at 2.0 V appears under the increasing current density of 20C due to structural rearrangements caused by the local heating at high current rates[51]. This similar phenomenon has been reported in other NASICON type materials[58]. Meanwhile, peak current of the NTP-rGO CV curves changes linearly with the increasing scan rates from 0.2 to 0.5 mV s^{-1} (**Fig. 5c**), demonstrating the fast, reversible charge storage

process. The discharge time of NTP-rGO at different current rates are much longer than that of NTP as shown in **Fig. S13†**. **Fig. 5d** displays the CV curves of NTP-rGO electrode for the initial four cycles at 0.5 mV s^{-1}, indicating remarkable reversibility and overlapping of the curves after the first cycle. To further demonstrate the cycle-stability of NTP-rGO, the cell was cycled for 250 cycles at 0.5 C (**Fig. 5e**). After 250 cycles, the discharge capacity retains at 114.9 mAh g^{-1}, corresponding to 91% capacity retention calculated on the initial capacity. In addition, even after 1000 cycles at the high current density of 10 C, the final discharge capacity is 92.0 mAh g^{-1} and the capacity fading is just 18% (**Fig. S14†**). It is noteworthy that the small capacity fading reveals the good stability and reversibility.

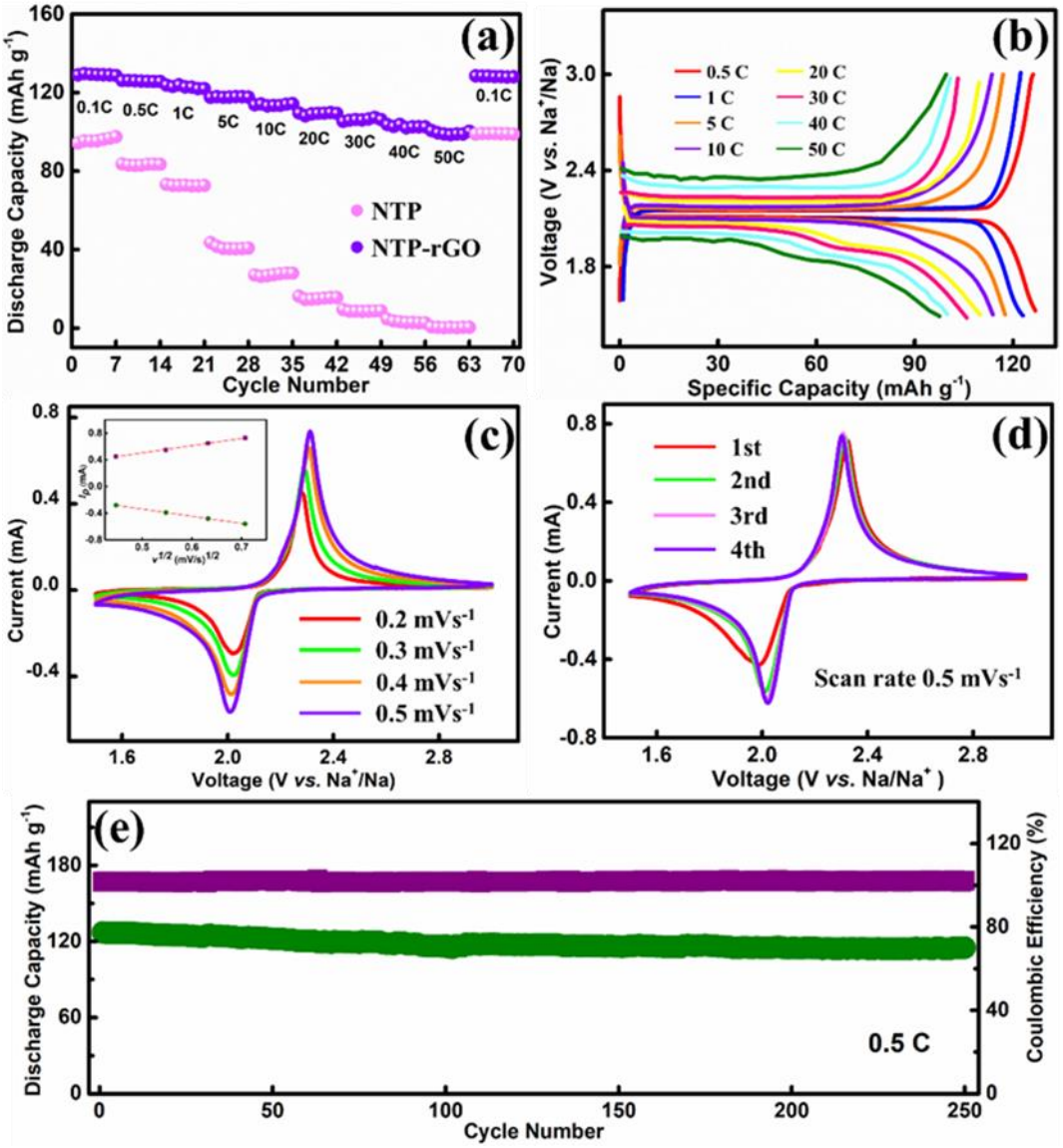

Fig. 5 a) The capacity of NTP materials as the cathode in a half-cell sodium battery tested at different current densities; b) Galvanostatic charge-discharge profiles of the NTP-rGO at different current densities; c) CV curves at different scan rates and the relationship between the I_p and $v^{1/2}$ (the inset); d) CV curves of the first four cycles under 0.5 mV s^{-1}; e) Long-term cycling performance at 0.5 C.

To further investigate the variation of Na^+ diffusion coefficient in the NTP-rGO anode, galvanostatic intermittent titration technique (GITT) measurement was performed at 0.1 C (**Fig. S15†**). The GITT curve for the charge process is shown in **Fig. S15a†**. And **Fig. S15b†** presents a single step of GITT curve. Upon the Fick's second law of diffusion and some relative assumptions and simplifications, the diffusion coefficient of Na^+ can be calculated by the following equation[59-60]:

$$D_{Na^+} = \frac{4}{\pi}\left(\frac{m_B V_M}{M_B A}\right)^2\left(\frac{\Delta E_s}{\tau(dE_\tau)/d\sqrt{\tau}}\right)^2 \quad (\tau \ll L^2/D_{Na^+}) \qquad (3)$$

where M_B, A, V_M, m_B and L represent the relative formula mass, the contact area between the electrolyte and electrode, the molar volume of the compounds, the active mass in electrode and the thickness of electrode, respectively. If E *vs.* $\sqrt{\tau}$ shows a straight-line behavior during titration (**Fig. S15c†**), the above-mentioned equation can be simplified as[61]:

$$D_{Na^+} = \frac{4}{\pi\tau}\left(\frac{m_B V_M}{M_B A}\right)^2\left(\frac{\Delta E_s}{\Delta E_\tau}\right)^2 \qquad (4)$$

On the basis of this equation, the D_{Na+} was calculated from the

GITT data during the charge process. The D_{Na+} values of the NTP-rGO anode are in the range from 10^{-14} to 10^{-11} cm^2s^{-1}, which are higher than that of NTP (10^{-15} to $10^{-11.5}$ cm^2s^{-1}) as shown in **Fig. S15d**†. As indicated by the GITT results, the structure of the NTP-rGO is beneficial for Na^+ diffusion process.

The *ex-situ* XRD technique is an effective means to understand the structure evolution of electrode materials during sodiation/desodiation[62]. **Fig. 6b** presents corresponding XRD patterns of NTP-rGO taken upon reduction at points labeled 1-6# in the discharge curve in **Fig. 6a**. Upon sodium insertion, a new set of peaks appear at 2θ = 20.1°, 23.6°, 32° and 35.2°, which can be well assigned to $Na_3Ti_2(PO_4)_3$[63]. These peaks gradually grow in intensity, while other peaks attributed to $NaTi_2(PO_4)_3$ gradually decrease in intensity and finally disappear at the stage of 6#. The *ex-situ* XRD measurements confirm the existence of $NaTi_2(PO_4)_3$ and $Na_3Ti_2(PO_4)_3$ in the sodiation process.

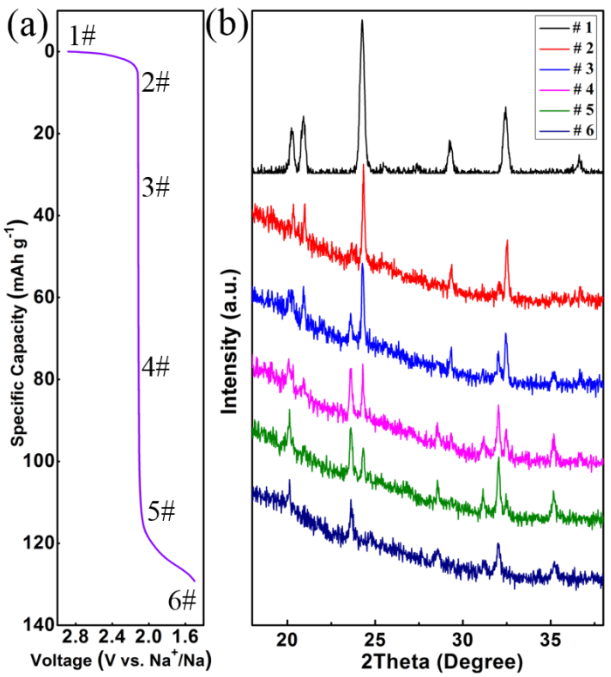

Fig. 6 a) Discharge curve of NTP-rGO at 0.1 C, b) XRD patterns recorded at different stages of discharge process of NTP-rGO.

The changes of NTP-rGO material in dynamic morphology can be visualized by the *in-situ* TEM experiments (**Fig. 7** and **Movie S1**, accelerated 32 times). The *in-situ* TEM images of NTP-rGO were collected at different time points during sodiation/desodiation process in **Fig. 7a-f**. No obvious morphology and volume changes are observed, which can be speculated as the stable structure. Similar to the case of NTP-rGO composite, the NTP also displays the small volume change in the process of sodiation/desodiation (**Fig. S16**†, **Movie S2**, accelerated 32 times). In addition, at the end of the sodiation process, $Na_3Ti_2(PO_4)_3$ phase appearance is confirmed according to its diffraction rings and lattice fringes by the SAED pattern (**Fig. 7h**), compared with the initial $NaTi_2(PO_4)_3$ material (**Fig. 7g**), which is in agreement with the *ex-situ* XRD results.

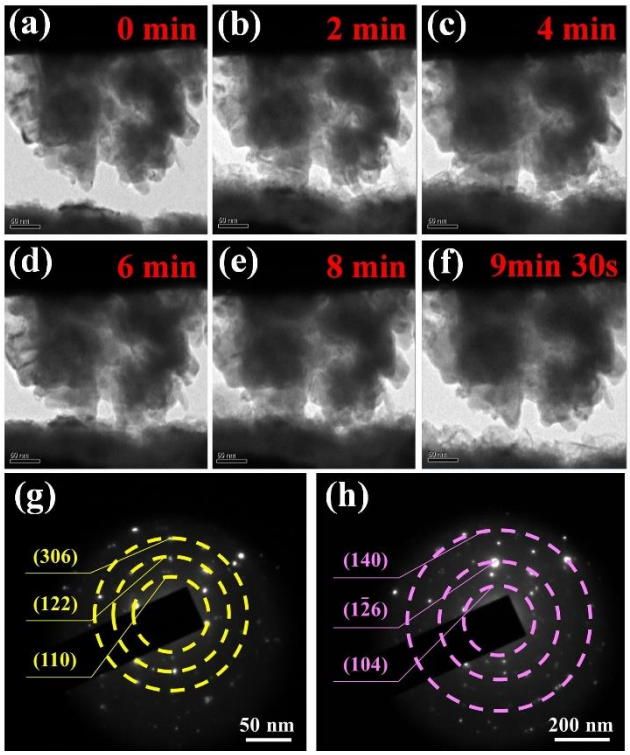

Fig. 7 a-f) *In-situ* TEM of the NTP-rGO during the sodiation/desodiation process; SAED pattern of the NTP-rGO g) before sodiation and h) after sodiation.

Conclusions

In summary, a facile and cost-effective strategy has been developed to synthesize NASICON type materials based on MOFs template by controlling the solvothermal time. Through *in-situ* GO self-assemble and subsequent carbonization process, rGO-decorated NASICON type NTP materials have been easily synthesized for the first time. Such architecture combines the advantages of NTP with fast sodium ion diffusion and rGO with high electron transport, which possesses synergistically enhanced electron/ion transport kinetics and enough buffer space for volume expansion. As a result, the NTP-rGO materials exhibit attractive sodium storage properties. Furthermore, this oriented formation process is clearly revealed and could be generalized to involve the use of numerous MOFs. Therefore, our work shows that MOF with unique characteristics for functionalization, is a suitable template for the development of NASICON type structure functional hybrid materials and can spark extensive interests in the exploration of novel electrode materials for constructing high performance energy storage systems.

Conflicts of interest

There are no conflicts to declare.

Author Contributions

Samples were prepared by Lei Wang and Luo Hao. Zhennan Huang performed the TEM measurement. Meng Cheng and Guijing Liu performed the SEM measurement. Yifei Yuan and Tara Foroozan performed the XRD measurement. Kun He

performed the XPS measurement. Ramasubramonian Deivanayagam performed the Raman measurement. Bo Wang Dianlong Wang and Reza Shahbazian-Yassar supervised the project.

Acknowledgements

Financial support from the National Natural Science Foundation of China (No. 51874110 and No.51604089), the Fundamental Research Funds for the Central Universities (Grant No. HIT.NSRIF.2017024), the China Postdoctoral Science Foundation (Grant No. 2016M601431 and 2018T110308), and the Heilongjiang Province Postdoctoral Science Foundation (Grant No. LBH-Z16056 and LBH-TZ1707) are gratefully acknowledged. R. Shahbazian-Yassar, T. Foroozan, M. Cheng, Y. Yuan, K. He, R. Deivanayagam and Z. Huang acknowledge the financial support from NSF DMR-1620901. Thank the China Scholarship Council for providing a scholarship (Grant No.201706120319).

Notes and references

[a]*MIIT Key Laboratory of Critical Materials Technology for New Energy Conversion and Storage, School of Chemistry and Chemical Engineering, Harbin Institute of Technology, 150001 Harbin, China. Fax: 86 45186413721; Tel: 86 45186413751; E-mail: wangbo19880804@163.com (B. Wang), wangdianlonghit@163.com (D. L. Wang)*

[b]*Department of Mechanical and Industrial Engineering, University of Illinois at Chicago, Chicago, IL 6068, USA. E-mail: rsyassar@uic.edu (R. Shahbazian-Yassar)*

[c]*School of Chemistry and Materials Science, Ludong University, Yantai, 264025, P R China*

† Electronic Supplementary Information (ESI) available: [details of any supplementary information available should be included here]. See DOI: 10.1039/b000000x/

1 H. Sun, L. Mei, J. Liang, Z. Zhao, C. Lee, H. Fei, M. Ding, J. Lau, M. Li, C. Wang, X. Xu, G. Hao, B. Papandrea, I. Shakir, B. Dunn, Y. Huang, X. Duan, *Science*, 2017, *356*, 599-604.

2 K.J. Griffith, K.M. Wiaderek, G. Cibin, L.E. Marbella, C.P. Grey, *Nature*, 2018, *559*, 556-563.

3 Y. Huang, M. Zhu, Y. Huang, Z. Pei, H. Li, Z. Wang, Q. Xue, C. Zhi, *Adv. Mater.*, 2016, *28*, 8344-8364.

4 F. Zhao, S. Shen, L. Cheng, L. Ma, J. Zhou, H. Ye, N. Han, T. Wu, Y. Li, J. Lu, *Nano Lett.*, 2017, *17*, 4137-4142.

5 P. He, Y. Fang, X.Y. Yu, X.W.D. Lou, *Angew Chem. Int. Ed. Engl.*, 2017, *56*, 12202-12205.

6 D.S. Bin, X.J. Lin, Y.G. Sun, Y.S. Xu, K. Zhang, A.M. Cao, L.J. Wan, *J. Am. Chem. Soc.*, 2018, *140*, 7127-7134.

7 D. Kundu, B.D. Adams, V. Duffort, S.H. Vajargah, L.F. Nazar, *Nat. Energy*, 2016, *1*.

8 N. Zhang, F. Cheng, J. Liu, L. Wang, X. Long, X. Liu, F. Li, J. Chen, *Nat. Commun.*, 2017, *8*, 405.

9 Q. Wang, X. Zhu, Y. Liu, Y. Fang, X. Zhou, J. Bao, *Carbon*, 2018, *127*, 658-666.

10 E. Gu, S. Liu, Z. Zhang, Y. Fang, X. Zhou, *J. Alloy. Compd.*, 2018, *767*, 131-140.

11 Y. Fang, X. Xu, Y. Du, X. Zhu, X. Zhou, J. Bao, *J. Mater. Chem. A*, 2018, *6*, 11244-11251.

12 Y.-Y. Wang, H. Fan, B.-H. Hou, X.-H. Rui, Q.-L. Ning, Z. Cui, J.-Z. Guo, Y. Yang, X.-L. Wu, *J. Mater. Chem. A*, 2018, *6*, 22966-22975.

13 L. Shi, D. Li, P. Yao, J. Yu, C. Li, B. Yang, C. Zhu, J. Xu, *Small*, 2018, *14*, e1802716.

14 Y. Zhao, Z. Wei, Q. Pang, Y. Wei, Y. Cai, Q. Fu, F. Du, A. Sarapulova, H. Ehrenberg, B. Liu, G. Chen, *ACS Appl. Mater. Inter.*, 2017, *9*, 4709-4718.

15 G. Pang, C. Yuan, P. Nie, B. Ding, J. Zhu, X. Zhang, *Nanoscale*, 2014, *6*, 6328-6334.

16 G. Li, Z. Yang, Y. Jiang, C. Jin, W. Huang, X. Ding, Y. Huang, *Nano Energy*, 2016, *25*, 211-217.

17 L. Zhang, X. Wang, W. Deng, X. Zang, C. Liu, C. Li, J. Chen, M. Xue, R. Li, F. Pan, *Nanoscale*, 2018, *10*, 958-963.

18 C. Masquelier, C. Wurm, J. Rodriguez-Carvajal, J. Gaubicher, L. Nazar, *Chem. Mater.*, 2000, *12*, 525-532.

19 Y. Jiang, X. Zhou, D. Li, X. Cheng, F. Liu, Y. Yu, *Adv. Energy Mater.*, 2018, *8*, 1800068.

20 W. Wang, B. Jiang, L. Hu, S. Jiao, *J. Mater. Chem. A*, 2014, *2*, 1341-1345.

21 C. Wu, P. Kopold, Y. Ding, P. Aken, J. Maier, Y. Yu, *ACS nano*, 2015, *9*, 6610-6618.

22 X. Rui, W. Sun, C. Wu, Y. Yu, Q. Yan, *Adv. Mater.*, 2015, *27*, 6670-6676.

23 L. Wang, B. Wang, G. Liu, T. Liu, T. Gao, D. Wang, *RSC Adv.*, 2016, *6*, 70277-70283.

24 G. Binitha, A. G. Ashish, D. Ramasubramonian, P. Manikandan, M. M. Shaijumon, *Adv. Mater. Interfaces* 2016, *3*, 1500419.

25 T. Foroozan, F. A. Soto, V. Yurkiv, S. S. Asl, R. Deivanayagam, Z. Huang, R. Rojaee, F. Mashayek, P. B. Balbuena, R. S. Yassar, *Adv. Funct. Mater.*, 2018, *28*, 1705917.

26 Y. Shao, M.F. El-Kady, L.J. Wang, Q. Zhang, Y. Li, H. Wang, M.F. Mousavi, R.B. Kaner, *Chem. Soc. Rev.*, 2015, *44*, 3639-3665.

27 D. Yu, K. Goh, H. Wang, L. Wei, W. Jiang, Q. Zhang, L. Dai, Y. Chen, *Nat. Nanotechnol.*, 2014, *9*, 555-562.

28 F. Cao, M. Zhao, Y. Yu, B. Chen, Y. Huang, J. Yang, X. Cao, Q. Lu, X. Zhang, Z. Zhang, C. Tan, H. Zhang, *J. Am. Chem. Soc.*, 2016, 138, 6924-6927.

29 E.A. Dolgopolova, A.J. Brandt, O.A. Ejegbavwo, A.S. Duke, T.D. Maddumapatabandi, R.P. Galhenage, B.W. Larson, O.G. Reid, S.C. Ammal, A. Heyden, M. Chandrashekhar, V. Stavila, D.A. Chen, N.B. Shustova, *J. Am. Chem. Soc.*, 2017.

30 Z. Liang, C. Qu, W. Guo, R. Zou, Q. Xu, *Adv. Mater.*, 2018, *30*, e1702891.

31 H. A. Ardakani, Y. Yuan, W. Yao, A. Nie, K. Amine, J. Lu, R. S. Yassar, *Small Methods*, 2017, 1700202.

32 Y. Yuan, K. Amine, J. Lu, R. S. Yassar, *Nature Communications*, 2017, *8*, 15806.

33 A. Nie, L. Gan, Y. Cheng, H. A. Ardakani, Q. Li, C. Dong, R. Tao, F. Mashayek, H. Wang, U. Schwingenschlogl, R. Klie, R. S. Yassar, *ACS Nano*, 2013, *7*, 6203–6211.

34 H. Ghassemi, M. Au, N. Chen, P. A. Heiden, R. S. Yassar, *ACS Nano*, 2011, *5*, 7805–7811.

35 H. Luo, B. Wang, T. Liu, F. Jin, R. Liu, C. Xu, C. Wang, K. Ji, Y. Zhou, D. Wang, S. Dou, *Energy Storage Materials*, 2018.

36 B. Zhao, Q. Wang, S. Zhang, C. Deng, *J. Mater. Chem. A*, 2015, *3*, 12089-12096.

37 X. Li, X. Zhu, J. Liang, Z. Hou, Y. Wang, N. Lin, Y. Zhu, Y. Qian, *J. Electrochem. Soc.*, 2014, *161*, A1181-A1187.

38 J. Ko, C. Choi, B. Dunn, J. L, *J. Electrochem. Soc.*, 2017, *164*, A2124-A2130.

39 Y. Fang, L. Xiao, J. Qian, Y. Cao, X. Ai, Y. Huang, H. Yang, *Adv. Energy Mater.*, 2016, *6*, 1502197.

40 J. Yang, J. Wang, D. Wang, X. Li, D. Geng, G. Liang, M. Gauthier, R. Li, X. Sun, *J. Power Sources*, 2012, *208*, 340-344.

41 J. Liu, J. Zhang, S. Cheng, Z. Liu, B. Han, *Small*, 2008, *4*, 1976-1979.

42 L. Jing, H. Tan, R. Amal, Y. Ng, K. Sun, *J. Mater. Chem. A*, 2015, *3*, 15675-15682.

43 O. Akhavan, E. Ghaderi, *Nanoscale*, 2013, *5*, 10316-10326.

44 G. Xu, Z. Li, X. Wei, L. Yang and P. K. Chu, *Electrochim. Acta*, 2017, *254*, 328-336.

45 Y. Jiang, L. Zeng, J. Wang, W. Li, F. Pan and Y. Yu, *Nanoscale*, 2015, *7*, 14723-14729.

46 G. Yang, H. Song, M. Wu and C. Wang, *J. Mater. Chem. A*, 2015, *3*, 18718-18726.

47 Z. Huang, L. Liu, L. Yi, W. Xiao, M. Li, Q. Zhou, G. Guo, X. Chen, H. Shu, X. Yang and X. Wang, *J. Power Sources*, 2016, *325*, 474-481.

48 G. B. Xu, L. W. Yang, X. L. Wei, J. W. Ding, J. X. Zhong and P. K. Chu, *J. Power Sources*, 2016, *327*, 580-590.

49 P. Wei, Y. Liu, Z. Wang, Y. Huang, Y. Jin, Y. Liu, S. Sun, Y. Qiu, J. Peng, Y. Xu, X. Sun, C. Fang, J. Han, Y. Huang, *ACS Appl. Mater. Inter.*, 2018, *10*, 27039-27046.

50 L. Xu, G. Xu, Z. Chen, X. Wei, J. Cao, L. Yang, *J. Mater. Sci.: Materials in Electronics*, 2018, *29*, 9258-9267.

51 M. Li, L. Liu, P. Wang, J. Li, Q. Leng, G. Cao, *Electrochim. Acta*, 2017, *252*, 523-531.

52 B. Wang, A. Liu, W.A. Abdulla, D. Wang, X.S. Zhao, *Nanoscale*, 2015, *7*, 8819-8828.

53 B. Wang, W. Al Abdulla, D. Wang, X.S. Zhao, *Energ. Environ. Sci.*, 2015, *8*, 869-875.

54 L. Perreault, F. Colo`, G. Meligrana, K. Kim, S. Fiorilli, F. Bella, J. Nair, C. Vitale-Brovarone, J. Florek, F. Kleitz, C. Gerbaldi, *Adv. Energy Mater.*, 2018, *8*, 1802438-1802450.

55 M. Chen, W. Xu, S. Jamil, S. Jiang, C. Huang, X. Wang, Y. Wang, H. Shu, K. Xiang, P. Zeng, *Small*, 2018, e1803134.

56 B. Wang, B. Xu, T. Liu, P. Liu, C. Guo, S. Wang, Q. Wang, Z. Xiong, D. Wang, X.S. Zhao, *Nanoscale*, 2014, *6*, 986-995.

57 Y. Jiang, J. Shi, M. Wang, L. Zeng, L. Gu, Y. Yu, *ACS Appl. Mater. Inter.*, 2016, *8*,689-695.

58 K. Saravanan, C. Mason, A. Rudola, K. Wong, P. Balaya, *Adv. Energy Mater.*, 2013, *3*, 444-450.

59 C.-H. Shen, S.-Y. Shen, F. Fu, C.-G. Shi, H.-Y. Zhang, M.J. Pierre, H. Su, Q. Wang, B.-B. Xu, L. Huang, J.-T. Li, S.-G. Sun, *J. Mater. Chem. A*, 2015, *3*, 12220-12229.

60 Y. Li, W.Q. Bai, D.H. Wang, X.Q. Niu, Y.D. Zhang, H. Tang, X.L. Wang, C.D. Gu, J.P. Tu, *Electrochim. Acta*, 2015, *161*, 252-260.

61 Y.Q. Qiao, J.P. Tu, X.L. Wang, J. Zhang, Y.X. Yu, C.D. Gu, *The J. Phys. Chem. C*, 2011, *115*, 25508-25518.

62 Y. Liu, X. -Y. Yu, Y. Fang, X. Zhu, J. Bao, X. Zhou, X. W. Lou, *Joule*, 2018, *2*, 725-735.

63 P. Senguttuvan, G. Rousse, M. E. A. Dompablo, H. Vezin, J. -M Tarascon, M. R. Palacin, *J. Am. Chem. Soc.*, 2013, *135*, 3897-3903.

Graphic abstract

The titanium-based metal-organic frameworks (MIL-125) have been used as an *in-situ* etching template for the titanium resource enabling them with a structure-controlled property for the self-assembly of graphene oxide (GO) to construct the $NaTi_2(PO_4)_3$ and rGO composite electrodes. Such architecture combines the advantages of NTP with fast sodium ion diffusion and rGO with high electron transport, which synergistically induce enhanced electron/ion transport kinetics and enough buffer space for volume expansion.